1996 2

(4)

Monitoring of Weld Joint Penetration Based on Weld Pool Geometrical Appearance

The geometrical appearance of the weld pool contains sufficient information to determine full joint penetration in GTAW

BY R. KOVACEVIC, Y. M. ZHANG AND L. LI

ABSTRACT. Weld joint penetration monitoring and control are fundamental issues in automated welding. A skilled human operator can determine the weld penetration from the geometrical appearance of the weld pool. To emulate this using machine vision, a high-shutter-speed camera assisted with pulsed laser illumination is used to capture the clear image of the weld pool. The pool boundary is extracted by the developed real-time image processing algorithm. In order to emphasize the emulation of the human operator, general terms, *i.e.*, size, shape and geometrical appearance, are used for the conceptual discussion, whereas more specific terms such as length, width, and rear angles are used in the detailed analysis. In particular, the size will be specified by the pool width and length, and the shape will be defined using the proposed rear angle of the weld pool. The geometrical appearance is described by a combination of the size and shape parameters. To investigate the relationships, which could be complicated, between the weld penetration and different parameters, neural networks are used because of their capability for modeling complicated nonlinear functions. Extensive experiments have been developed to measure the weld penetration from the captured image in 200 ms using the neural network and real-time image processing.

R. KOVACEVIC, Y. M. ZHANG AND L. LI are with the Welding Research and Development Laboratory, Center for Robotics and Manufacturing Systems and Department of Mechanical Engineering, University of Kentucky, Lexington, KY.

Introduction

The sensing of weld joint penetration is a fundamental issue in automated welding. The concern is the measurement of the root surface (backside) bead width and depth of penetration in the full and partial penetration modes, respectively. In principle, these parameters can be monitored by embedding thermocouples into the weldment or by acoustic emission sensing (Refs. 1, 2). However, their practical applications are limited because of the contact between the sensors and the workpiece. In the case of full joint penetration, the root face width can be detected by measuring the light intensity from the backside (Refs. 3–5). However, it is difficult or impossible to conveniently locate backside sensors for many configurations, for instance, during the welding of pressure containers. Also, the motion match between the torch and sensor could be difficult if the torch moves. Hence, the sensor should be attached to and move with the torch to conduct the so-called topside sensing of the weld joint penetration. In this study, topside sensing is addressed.

KEY WORDS

GTAW
Weld Joint Penetration
Weld Pool
Sensors
Real-Time Image Processing
Neural Networks
High-Shutter-Speed Camera
Laser Illumination

Among the many proposed topside sensing techniques, pool oscillation methods have been extensively studied. The pioneering work was done by Richardson (Ref. 6), Hardt (Ref. 7), and their coworkers. Wang, *et al.*, found that for full penetration, the width of a stationary weld pool can be determined by the resonance frequency (Ref. 8). An interesting discovery was the distinction between the partial joint penetration and full joint penetration frequencies. Xiao and Ouden (Refs. 9, 10) found that a drop in the oscillation frequency occurs as the penetration state changes from partially penetrated to sufficiently penetrated. This frequency drop has also been observed by Richardson and Yoo (Ref. 11). For the measurement of the pool oscillation, both arc voltage and arc light fluctuations have been used (Refs. 6, 12).

Ultrasonic testing has become a standard technique for locating cracks, incomplete fusion, porosity and other discontinuities in fusion welds (Ref. 13). For a single point range measurement, the problem is to measure the transit time for a single ultrasound pulse to travel to and from the reflector, which is a discontinuity in material property. Theoretically, if the dimension of the reflector (for instance, crack, porosity, etc.) is larger than the wavelength of the incident ultrasound pulse, the reflected pulse contains information concerning the size and shape of whatever caused the reflection. Since the weld pool constitutes a change in phase and in material properties rela-

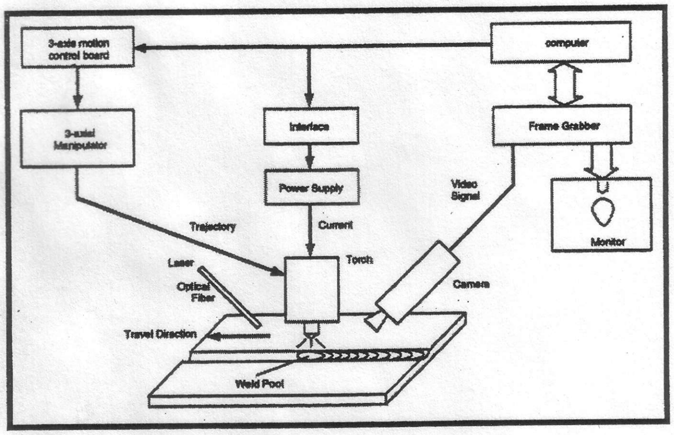

Fig. 1 — Experimental setup.

tive to the unmolten weldment, its shape and size may be measured through its reflected ultrasound. Hardt and Katz (Ref. 13) utilized reflection ultrasound methods to measure the size of the stationary weld pool. In their investigation, a simplified weldment geometry (a cylindrical rod) combined with a ray optics wave analysis was used. The propagation of the ultrasound in this cylindrical rod was studied. The results showed good agreement between the measurements performed on the cylindrical rods and the geometric optics prediction. Ultrasonic measurements of the weld pool were extensively studied at the Idaho National Engineering Laboratory (Refs. 14, 15). Different geometries of welds were distinguished (Ref. 15). Contact transducers were used. When the ultrasound was generated by a pulsed Nd:YAG laser, the contact transducer could be eliminated (Ref. 16). However, several new problems, including the surface damage, were caused (Ref. 17). For the post measurement of the depth of the weld pool, excellent results have been acquired by using laser-phased-array technology (Ref. 17).

Modern infrared thermograph equipment provides a feasible means to measure the temperature field. At Auburn University, the infrared sensing of arc welding processes has been extensively investigated by Chin and coworkers (Refs. 18–20). The temperature distribution is measured in gas metal arc welding (Ref. 20). It was found that the depth of joint penetration can be determined using the characteristics of the temperature profiles. Beardsley, *et al.*, found that the root surface bead width of the full joint penetration welds can be determined in gas tungsten arc welding using the pool area and a ratio between a surrounding area (600°C isotherm area) of the weld pool and the weld pool area (Ref. 21).

Despite the above achievements in the topside sensing of weld joint penetration, more accurate information can still be expected from the weld pool itself. It is known that the weld pool contains abundant information on the welding process. By viewing the weld pool, a skilled operator can estimate the weld joint penetration. However, detailed studies should be done to verify that the weld pool does contain sufficient information on the weld penetration. If this is true, an approach may be developed to measure the weld penetration using the parameters of the weld pool.

The weld pool has been coaxially viewed by Richardson, *et al.* (Ref. 22). The principle behind this technology is that the reflection of the arc light from the mirror-like pool surface is primarily specular. The diffuse reflection of the arc light is weaker from the weld pool than it is from the surrounding area. The weld pool is therefore expected to produce a dark area in the image, whereas the solid area should appear bright. This does in fact occur, however, the intensity contrast between the pool and the surrounding area is not very pronounced, due to the radiation from the pool.

In this study, a high-shutter-speed camera assisted with a pulsed laser (Ref. 23) is used. Clear images of the weld pool are captured. The pool boundary is extracted in real-time using the developed image processing algorithm. The rear angle is proposed to describe the shape of the weld pool. The geometrical appearance of the weld pool is characterized by the rear angles and length of the weld pool. To emulate the human operator in extracting the weld penetration, artificial neural networks are utilized. The feature parameters of the weld pool are input into the network and the weld penetration is calculated as the output. It is shown that the geometrical appearance of the weld pool contains sufficient information on the weld penetration. A real-time system has been developed to monitor the weld penetration using the geometrical appearance of the weld pool.

It should be pointed out that the efforts in this study have been limited to using the two-dimensional geometrical information from the weld pool. The three-dimensional topography of the weld pool surface may also be used to determine the weld penetration. Previous investigators have shown that the pool sag or the pool depression is correlative to the weld penetration (Refs. 24, 25). However, sensing the three-dimensional pool surface was difficult. It was found that the sag of the weld behind the pool rear has

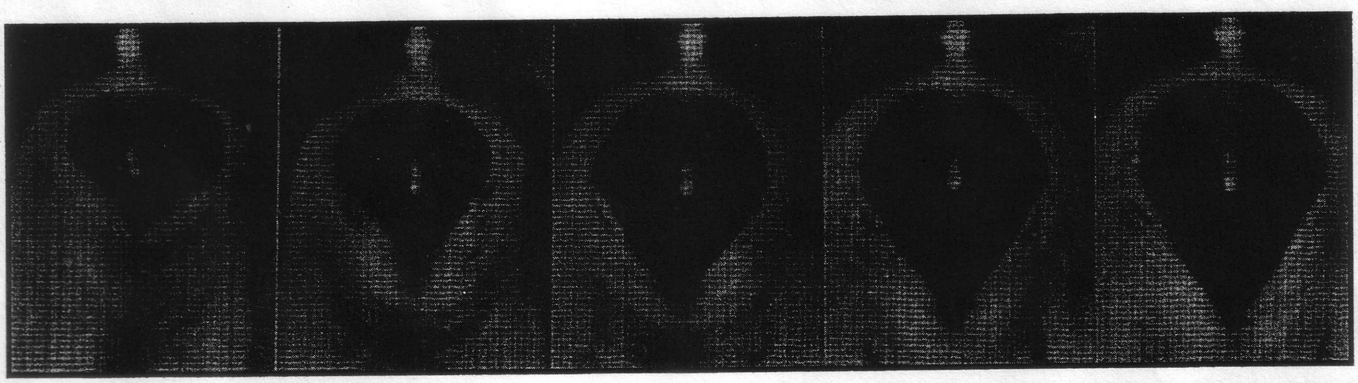

Fig. 2 — Weld pools for different currents. Arc length = 3 mm, travel speed = 1.9 mm/s, bead-on-plate, rate of argon flow = 30 ft^3/h, 304 stainless steel, 3 mm thickness. A — Current = 90 A, full penetration, backside bead width 1.8 mm; B — current = 95 A, full penetration, backside bead width 3 mm; C — current = 105 A, full penetration, backside bead width 4 mm; D — current =110 A, full penetration, backside bead width 4.5 mm; E — current = 115 A, full penetration, backside bead width 5 mm.

a good relationship with the root face bead width (Ref. 26). Thus, as an alternative, a vision-based adaptive system was developed to monitor and control the sag geometry for achieving the desired root face bead width (Refs. 27, 28). Recently, the authors have developed a specular reflection-based vision system to directly monitor the three-dimensional topography of the weld pool surface (Refs. 29–31). Although the pool depression may be directly controlled to achieve the desired weld penetration using this novel technology, the image processing algorithm for detecting the three-dimensional weld pool surface is much more complicated than the algorithm for the two-dimensional boundary of the weld pool. Hence, as the first step, this work will focus on the two-dimensional domain.

Experimental Procedure

Experimental Set Up

The experimental system is shown in Fig. 1. The welds are made using direct current electrode negative (DCEN) gas tungsten arc welding. The welding current is controlled by the computer (Pentium 90) through a D/A board output to the power supply ranged from 10 A to 200 A. The torch and camera are attached to a three-axial manipulator. The motion of the manipulator is controlled by the three-axis motion control board, which receives the commands from the computer. The motion can be preprogrammed and modified on-line by the computer to achieve the required torch speed and trajectory, including the arc length.

The camera is positioned directly behind the weld pool with its axis at a 45-deg angle from the horizontal. The laser is projected from the front of the weld pool with an incident angle of 50 deg, thus avoiding the bright specular reflection in the image. The frame grabber digitizes the video signal into 512 x 512 8-bit digital image matrix. To acquire a quality image for extracting the pool boundary, a high-shutter-speed camera assisted with a pulsed laser is used. The pulse of the laser lasts only 3 ns. The shutter of the camera is synchronized with the laser pulse. Although the average power of the laser is only 7 mW, its peak power reaches 70 kW. During the pulse duration, the intensity of the laser illumination is much stronger than those of the arc and hot metal. Thus, the area illuminated by the laser will be bright in the image. However, the weld pool will be dark since the projected laser is specularly reflected from the mirror-like weld pool surface. Consequently, clear images as shown in Fig. 2 can be acquired.

Table 1 — Experimental Conditions

No.	Current (A)	Arc Length (mm)	Speed (mm/s)	Duration (seconds)	Ar Flow Rate (ft^3/h)
1	100	see Fig. 3A	1.9	100	30
2	100	see Fig. 3B	1.9	100	30
3	see Fig. 3C	3	1.9	100	30
4	100	3	1.9	100	25
5	100	3	2.92	65	30
6	100	3	2.41	80	30
7	100	3	1.43	130	35
8	100	3	1.95	100	30

Experimental Conditions

Variation in weld joint penetration could be generated by changing welding parameters, such as the welding current, arc length, and travel speed, and welding conditions such as the root opening or geometry of the groove, material, thickness, workpiece size, heat transfer condition, electrode angle, and rate of the shielding gas flow. In order to form a valid method to monitor the weld penetration, the major parameters that may vary during welding should be considered in the experiments. Three-millimeter-thick stainless steel (304) plates are used without any specific surface preparation. The shielding gas is pure argon. The electrode is 3 mm in diameter with a 60-deg tip angle. Bead-on-plate welds are made. The objective is to monitor the full penetration state which is described by the root face bead (backside) width. Varied current, arc length, and travel speed are selected to make the root face bead width vary in the range of interest. The detailed experimental conditions can be seen in Table 1 and Fig. 3.

Observation and Rear Angle

It is known that when the current or arc length increases, the pool width increases. However, the resultant changes in weld penetration are opposite. This implies that the pool width alone may not be sufficient for representing the weld penetration in some specific cases. To describe the weld penetration, additional parameters must be considered. Figure 2 shows the weld pools made with different currents. With the increase of the current, the root face bead width increases. It is seen that the length of the weld pool keeps increasing with the current, whereas the variation in the pool width is less significant. Also, as the weld penetration increases, the tail of the weld pool becomes sharply pointed. Thus, the length and sharpness of the weld pool could be used to represent the weld penetration.

To describe the sharpness of the weld

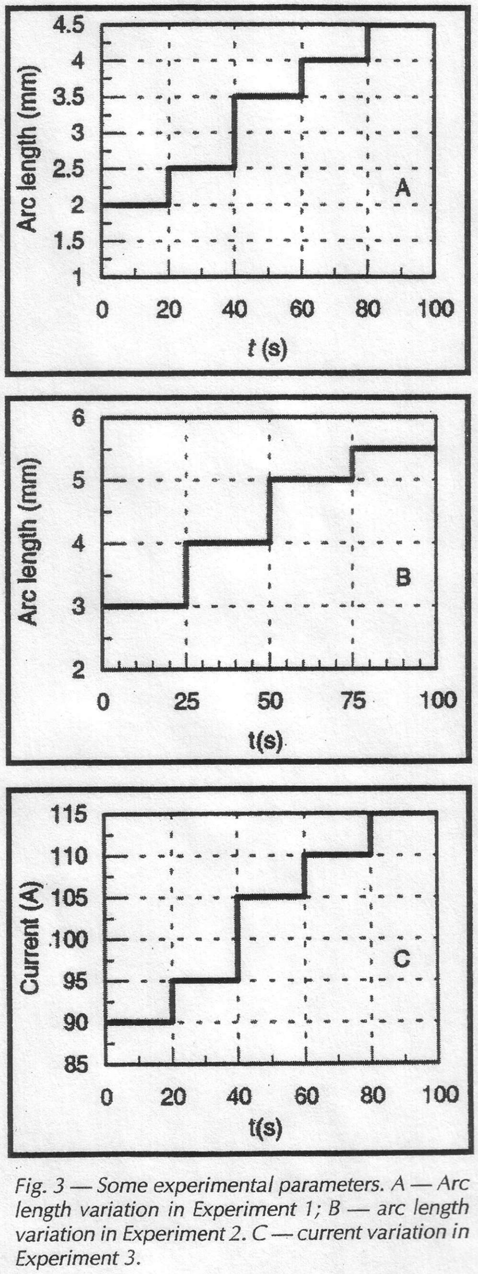

Fig. 3 — Some experimental parameters. A — Arc length variation in Experiment 1; B — arc length variation in Experiment 2. C — current variation in Experiment 3.

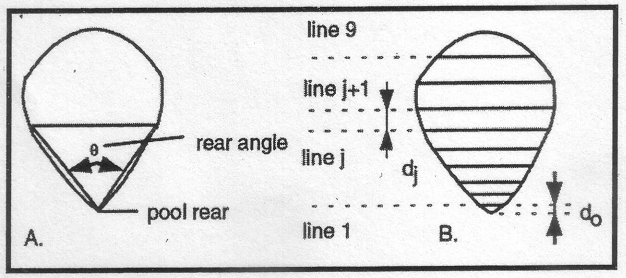

Fig. 4 — Rear angle and its computation. A — Definition; B — transverse lines for the computation of rear angles.

pool, the rear angle is proposed. Take the rear of the weld pool as the reference point — Fig. 4A. Draw a line along the transverse direction to cross the weld pool at a specific location along the length of the pool. Two intersections between the boundary of the weld pool and the line will be generated. Connect these two intersections with the reference point to generate two new lines. The angle between these two lines is defined as the rear angle of the weld pool (Fig. 4A). It is apparent that the rear angle depends on the selected location along the length of the weld pool.

In order to sufficiently describe the shape of the weld pool, nine rear angles are used for each weld pool at nine specific locations along the length of the weld pool — Fig. 4B. It is found that as the specific location of the transverse line approaches the reference point, *i.e.*, the weld pool rear, the role of the corresponding rear angle becomes more significant in determining the penetration state. In fact, the shape of the front of the weld pool does not change much with varying penetration. Thus, more rear angles should be acquired from the rear portion of the pool. Denote the length of the weld pool as L. The distance for line j to line j + 1 is $d_j = d_0 b^j$ (j = 1,...,9) where d_0 is the distance from the rear to the first line and b > 1 is the incremental ratio — Fig. 4B. It can be shown that d_j can be calculated using the following formula:

$$d_j = Lb^j (1-b)/(1-b^{10}) \qquad (1)$$

In this study, b is selected to be 1.3. The resultant nine lines for generating the rear angles are plotted in Fig. 4B. Thus, the nine rear angles can be calculated from the length and boundary of the weld pool.

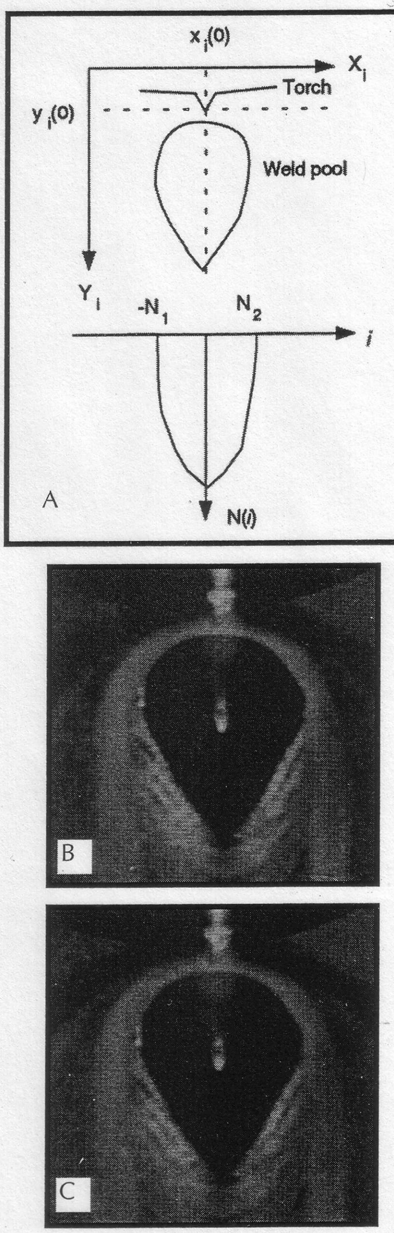

Fig. 5 — Image compression, binarization, and windowing. A — Windowing principle; B — binary image and x_i direction windowing; C — resultant compression, binarization and windowing. The compressed binary images are shown in the lower left corner of images. The size difference between the original and compressed images shows the compression ratio.

Data Processing

Image Processing

In a previous work, a real-time image processing algorithm was developed to extract the boundary of the weld pool (Ref. 32). To reduce the computation, dynamic search procedures were conducted. Although this algorithm can successfully extract the boundary of the weld pool in real-time, its programming is complicated. For convenience in implementation and application, a modified algorithm is proposed. Using this algorithm, the robustness and speed can also be improved. The boundary of the weld pool can be extracted in 60 ms from the acquired image despite the variations in surface and welding conditions.

The proposed algorithm consists of four steps: 1) image binarization, compression, and windowing, 2) edge detection, 3) boundary identification, and 4) fine search. In the first three steps, a rough boundary is acquired in order to improve the robustness and processing speed. Based on the rough boundary, a fine search can be done to find the accurate boundary of the weld pool with slight additional computation.

Assume that the axis of the electrode is $x_i = x_i(0)$, which can be determined before welding — Fig. 5A. The weld pool lies under $y_i = y_i(0)$ — Fig. 5A. In the first step, the captured image is scanned from $x_i(0)$ at $(x_i(0) + i\gamma)$'s (i = 0,1,2,...) along the x_i direction and at $(x_i(0) + i\gamma)$'s (i = −1,−2,...) along the negative x_i direction, respectively — Fig. 5A. The positive integer γ is the image compression factor which is taken as 4 in this study. During the scanning at $x_i = x_i(0) + i\gamma$, the image points at $(x_i(0) + i\gamma,\ y_i(0) + j\gamma)$'s (j = 0,1,2,...) are binarized. The number of dark pixels are accounted as N(i). It is evident that N(i) should be very small when $x_i = (x_i(0) + i\gamma)$ exceeds the pool range. Thus, the range of the weld pool along the horizontal direction, *i.e.*, $(-N_1 \le i \le N_2)$, can be roughly acquired without excessive computation, in addition to the binarization — Fig. 5B. Using the compressed binary image within $(-N_1 \le i \le N_2)$, a rough estimate of the range along the vertical direction can also be obtained — Fig. 5C. The resultant window can be described by the range $(-N_1 \le i \le N_2, M_1, \le j \le M_2)$ where N_1, N_2, M_1, and M_2 are all positive integers. The compressed binary image and resultant window are shown in Fig. 5C.

In the second step, the left and right edge points of the weld pool are searched from $i = -N_1$ and $i = N_2$, respectively, with increasing and decreasing i for a given j, respectively. It is known that both the left and right edge points should be located at transitions from the bright to dark areas during the searches. To exclude possible small dark areas caused by the severe oxidation in the solidified region due to the possible imperfect shielding, the search is continued for a few more pixels once the transition is encountered. If the succeeding pixels are dark, the transition is taken as the edge point. Otherwise, the transition is considered as the edge of a severely oxidized region and the search is continued. Thus, the weld pool edge can be detected despite small severely oxidized regions on the solidified surface.

It is observed that in some cases with extremely poor shielding, a large oxidized region could appear — Fig. 6A. In such a case, the edge of the oxidized region will be extracted — Fig. 6A. However, the horizontal coordinates of these points are close to $-N_1$ or N_2. Thus, if the edge points vary in a small range close to $-N_1$ or N_2, one should check whether or not any large bright region (in the binary image acquired in the first step) exists between the extracted left and right edges. If such large bright regions do exist, dark regions should be detected. Each dark region can be one candidate for the weld pool region. Thus, for some j, two or three dark regions may exist as the candidates for the weld pool. The left and right edges of the weld pool can be known — Fig. 6B. Based on the width of the region and how it changes with j, the weld pool region can be recognized. Thus, the edges of the weld pool can be acquired — Fig. 6C.

Assume that $edge_l(j)$'s ($j = M_1, M_1+1, \ldots M_2$) and $edge_r(j)$'s ($j = M_1, M_1+1, \ldots M_2$) are the acquired horizontal coordinates for the left and right edge points. Both $edge_l(j)$'s ($j = M_1, M_1+1, \ldots M_2$) and $edge_r(j)$'s ($j = M_1, M_1+1, \ldots M_2$) may not be continuous with j. In the third step, $edge_l(j)$'s ($j = M_1, M_1+1, \ldots M_2$) and $edge_r(j)$'s ($j = M_1, M_1+1, \ldots M2$) are segmented. If a continuous segment is short or has a large variation, *i.e.*, the magnitude of $d\,edge_l(j)/dj$ is large, this segment may not be caused by the actual boundary of the weld pool. To eliminate possible error, such segments are deleted. Only the actual pool boundary points remain — Fig. 6D. Because of the continuity of the weld pool, the number of deleted points is much smaller than the number of remaining points. Thus, if the points are used to fit models, the corresponding reduction of the fitting accuracy will be very slight.

Two polynomials can be fitted for the left and right edges, respectively. The parameters in the following models, *i.e.*, ($a_l(0), a_l(1), \ldots, a_l(p)$) and ($a_r(0), a_r(1), \ldots, a_r(p)$) need to be identified from the remaining data:

$$\left.\begin{array}{l} edge_l(j) = a_l(0) + \\ \sum_{k=1}^{p} a_l(k) j^k \\ edge_r(j) = a_r(0) + \\ \sum_{k=1}^{p} a_r(k) j^k \end{array}\right\} \quad (2)$$

where p is the order which is selected to be 4 based on modeling experimentation. The least squares algorithm (Ref. 33) has been used to identify the parameters. The fitted edges are illustrated in Fig. 6E. It can be seen that despite the poor condition, correct estimates of the weld pool edges have been acquired from the compressed image.

The rough edge acquired in the compressed image can be restored to the original image — Fig. 7A. In the fourth step, the final pool edge is searched around the rough edge. Thus, the final pool boundary as shown in Fig. 7B can always be obtained. Based on this edge, the required parameters of the weld pool can be calculated.

The above four steps can be completed by our equipment in 30 to 60 ms. To sample the image, 33 ms is required. Thus, the weld pool boundary can be acquired at 10 Hz.

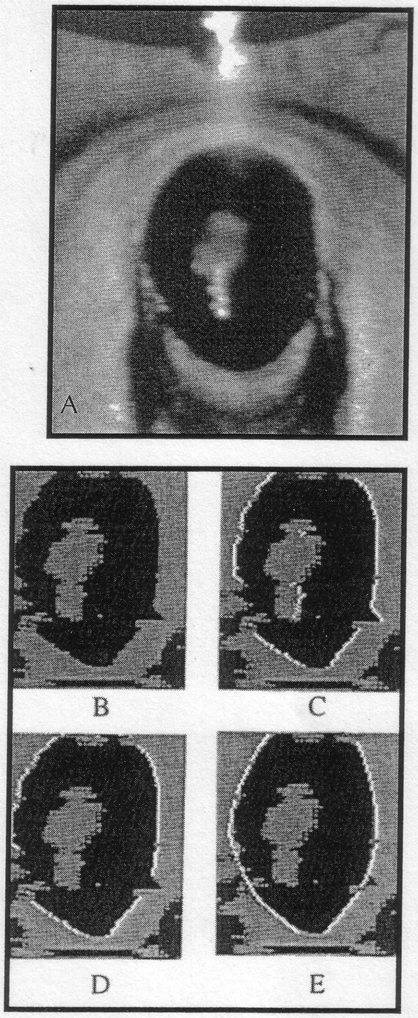

Fig. 6 — Edge detection for the image with severe oxidation. A — Original image; B — pool region candidates; C — edge points; D — remaining edge points; E — fitted edge. The edge detection is performed on the compressed binary image.

Coordinate Transformation

The boundary extracted by the image processing is described using the image coordinate. To acquire the actual geometrical appearance of the weld pool, the boundary should be described in the work coordinate system. The xy plane of the work coordinate system is the work surface and the z-axis is the electrode — Fig. 8. A transformation from the image coordinates to the work coordinates must be done.

Assume that $(x_i(j), y_i(j))$'s are the image coordinates of the boundary of the weld pool. The pool boundary $(x(j), y(j), z(j))$'s must be calculated from the $(x_i(j), y_i(j))$'s Since the work surface has been selected

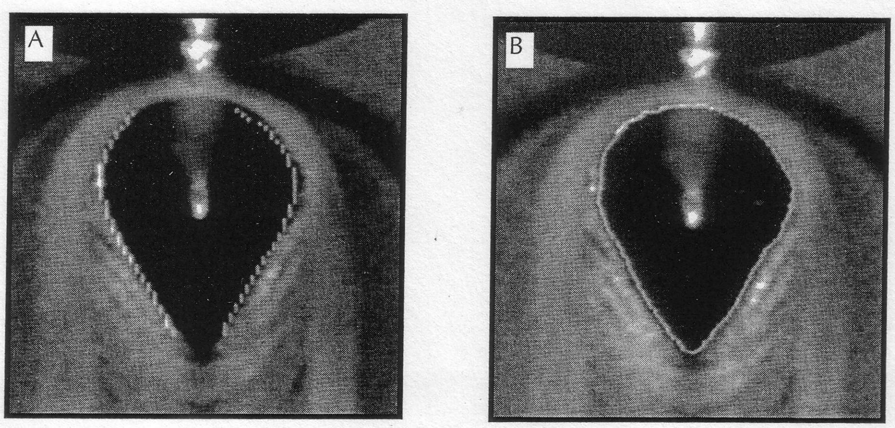

Fig. 7 — Fine search for the weld pool boundary. A — Restored rough edge; B — final result of the pool boundary.

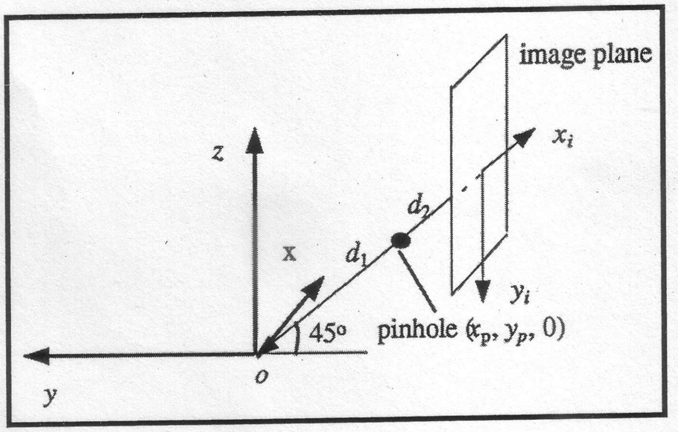

Fig. 8 — The relationship between the work and image coordinate systems. The work coordinate system is xyz. The image coordinate system is $x_i\ y_i$.

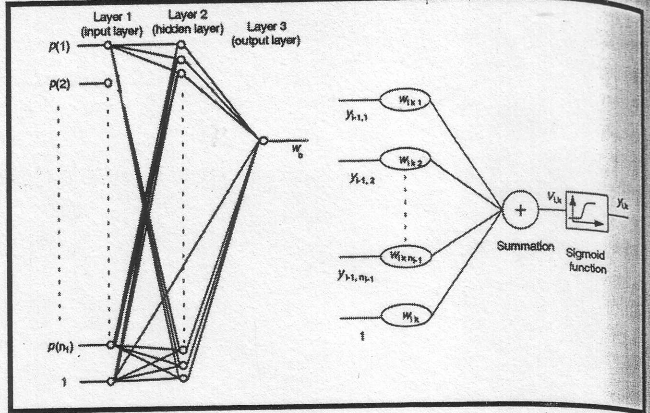

Fig. 9 — Neural network model for the weld penetration prediction. $p(j)$'s ($j = 1,...,n_1$) are the parameters of the weld pool selected as the inputs of the network. The output w_b of the network is the backside bead width. A — Architecture.; B — neuron structure.

to be the xy plane, the z(j)'s can be considered as zero. It can be shown that:

$$\left.\begin{array}{l} y(j)=y_p-z_p/tg \\ \left[45°-tg^{-1}\left(y_i(j)/d_2\right)\right] \\ x(j)=-x_i(j) \\ \left[y_i(j)+\sqrt{2d_l}\right]/\sqrt{2d_2} \end{array}\right\} \quad (3)$$

where (0, y_p, z_p) are the pinhole of the camera in the work coordinate system, d_1 is the distance from the origin of the work coordinate system to the pinhole, and d_2 is the distance from the origin of the camera coordinate system to the pinhole. The optical axis of the camera lies on the yz plane and the angle between the optical axis and the y axis is 45 deg. Thus, using the image processing results, *i.e.*, (x_i(j),y_i(j))'s, the boundary of the weld pool (x(j), y(j),z(j))'s can be acquired.

Modeling

In order to achieve accurate predictions of the weld penetration, nonlinear models, rather than linear models, are used to correlate the weld pool parameters with the weld penetration. However, the structure of the nonlinear relationships are very difficult to determine. Neural networks provide a uniform model frame for almost all types of nonlinear relationships. Thus, a neural network can be used to relate the pool parameters to the weld penetration.

For most applications, one hidden layer is sufficient (Ref. 34). In order to guarantee the validity of the resultant model, the number of elements in the hidden layer, denoted as n_2, is selected by the following equation (Ref. 34):

$$n_2 = N/10(n_1+n_3)\sim N/5(n_1+n_3) \quad (4)$$

where N is the number of samples, and n_1 and n_3 are the number of elements in the input and output layer, respectively.

The number of samples for each network is 7350. Different pool parameters will be used as the inputs of the network to calculate the backside bead width, which is the output of the neural network. Thus, the number of elements in the hidden layer will depend on the number of pool parameters used in the network. The general architecture of the resultant network is shown in Fig. 9A. The sigmoidal function (Ref. 35) is selected as the nonlinear function of the neuron which is shown in Fig. 9B. It is known as the following (Ref. 35):

$$\left.\begin{array}{l} y_{i,k}=1/\left(1+e^{-v_{ik}}\right) \\ v_{ik}=w_{ik}+\sum_{j=1}^{n_{i-1}} w_{ikj}y_{i-1,j} \end{array}\right\} \quad (5)$$

where $y_{i,k}$ is the output of the k^{th} neuron (element) in layer i, n_i is the number of neurons in layer i, and w_{ik} and w_{ikj} are the weights of the neuron which must be determined by the training process.

The training was performed using the commercial neural network software, Professional II (Ref. 34). The algorithm is the extended delta-bar-delta (EDD), which can overcome the slow convergence associated with the conventional back-propagation algorithm (Ref. 34). The learning ratio is automatically determined by the algorithm. The training cycle is selected to be 50,000.

Modeling Results

The pool feature parameters, including the length, width, and rear angles of the weld pool, are measured on-line during the experiments (Table 1) at the speed of 10 Hz. The backside width is measured off-line using a structured light vision system developed in a previous study (Ref. 36). The data in the first three seconds and last two seconds are deleted for each experiment. The resultant data is plotted in Fig. 10. It can be seen that the backside bead widths vary in a wide range, from 1 to 7 mm. The variation is caused by the different welding parameters or conditions. To monitor the weld penetration, this variation must be calculated with sufficient accuracy using the measurements of the pool feature parameters. For the thickness of the material used in this study, the required backside bead width may be selected between 2 and 5 mm so that the allowed error in determining the backside bead width should be less than 1 mm. For the convenience of the discussion, 1 mm is referred to as the critical measurement for the sufficiency of the modeling accuracy in this study.

All the pool parameters have been used as the inputs of the network for modeling the backside bead width. The number of elements in the hidden layer is selected to be 45 based on Equation 4. Using the trained network, the backside bead width can be calculated from the pool feature parameters. Figure 11A illustrates the calculated values, compared with the original measurements. It is found that the backside bead width can be traced with sufficient accuracy for different welding conditions, judged by the 1-mm critical measurement. This demonstrates that enough information on the full penetration state is contained in the selected pool parameters.

The weld pool could be characterized using three types of parameters, *i.e.*, size, shape, and geometrical appearance, from different points of view. The corresponding parameters are categorized as size, shape, and geometrical appearance parameters. The geometrical appearance

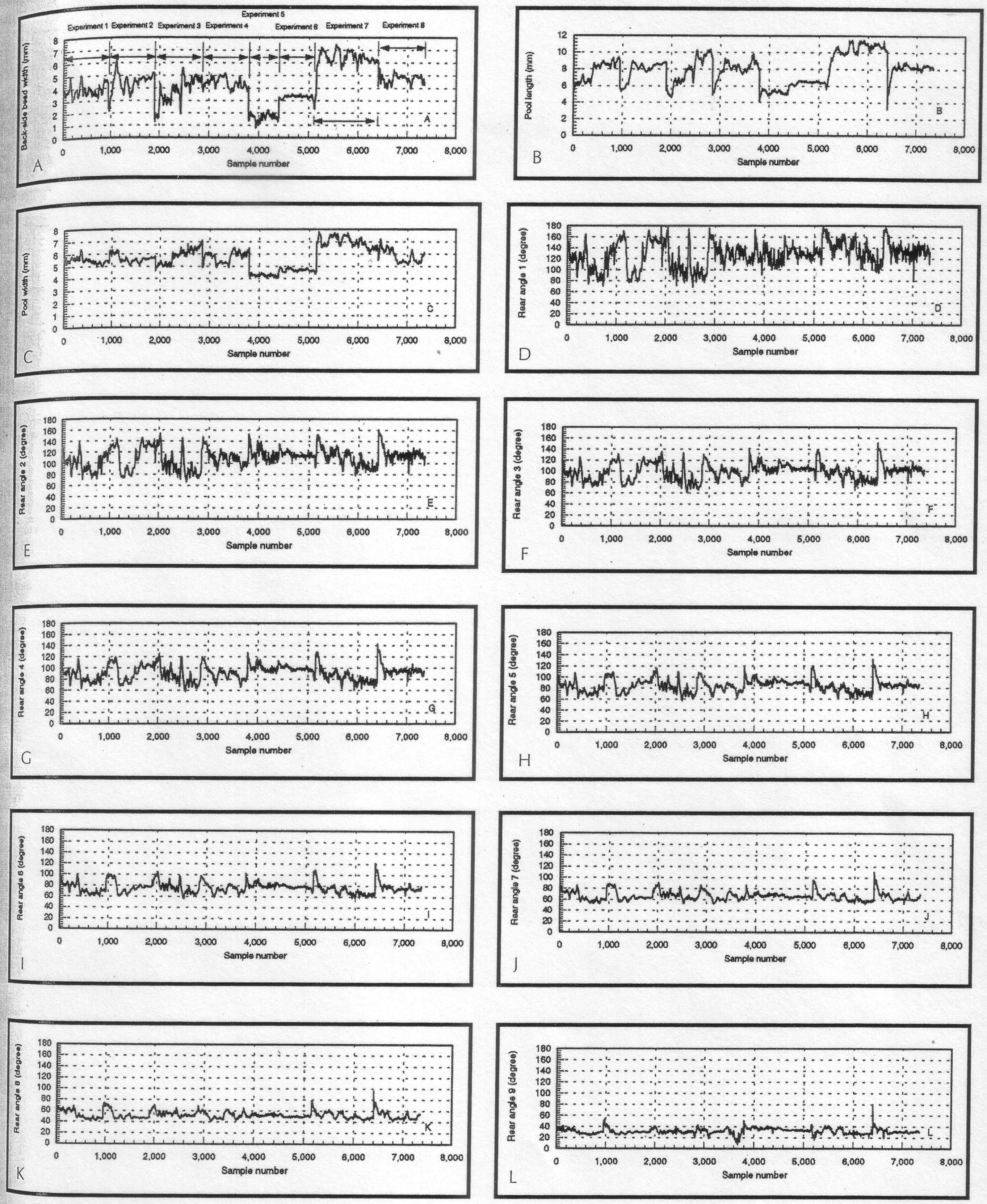

Fig. 10 — Experimental measurements. The data are arranged according to their serial number in the experiments (Table 1). The ranges of the sample number for each experiment are: No. 1 from 1 to 950; No. 2 from 951 to 1900; No. 3 from 1901 to 2850; No. 4 from 2851 to 3800; No. 5 from 3801 to 4400; No. 6 from 4401 to 5150; No. 7 from 5151 to 6400; No. 8 from 6401 to 7350. A — Backside bead width; B — length of weld pool; C — width of weld pool; D — rear angle θ_1; E — rear angle θ_2; F — rear angle θ_3; G — rear angle θ_4; H — rear angle θ_5; I — rear angle θ_6; G — Rear angle θ_7; K — rear angle θ_8; L — rear angle θ_9.

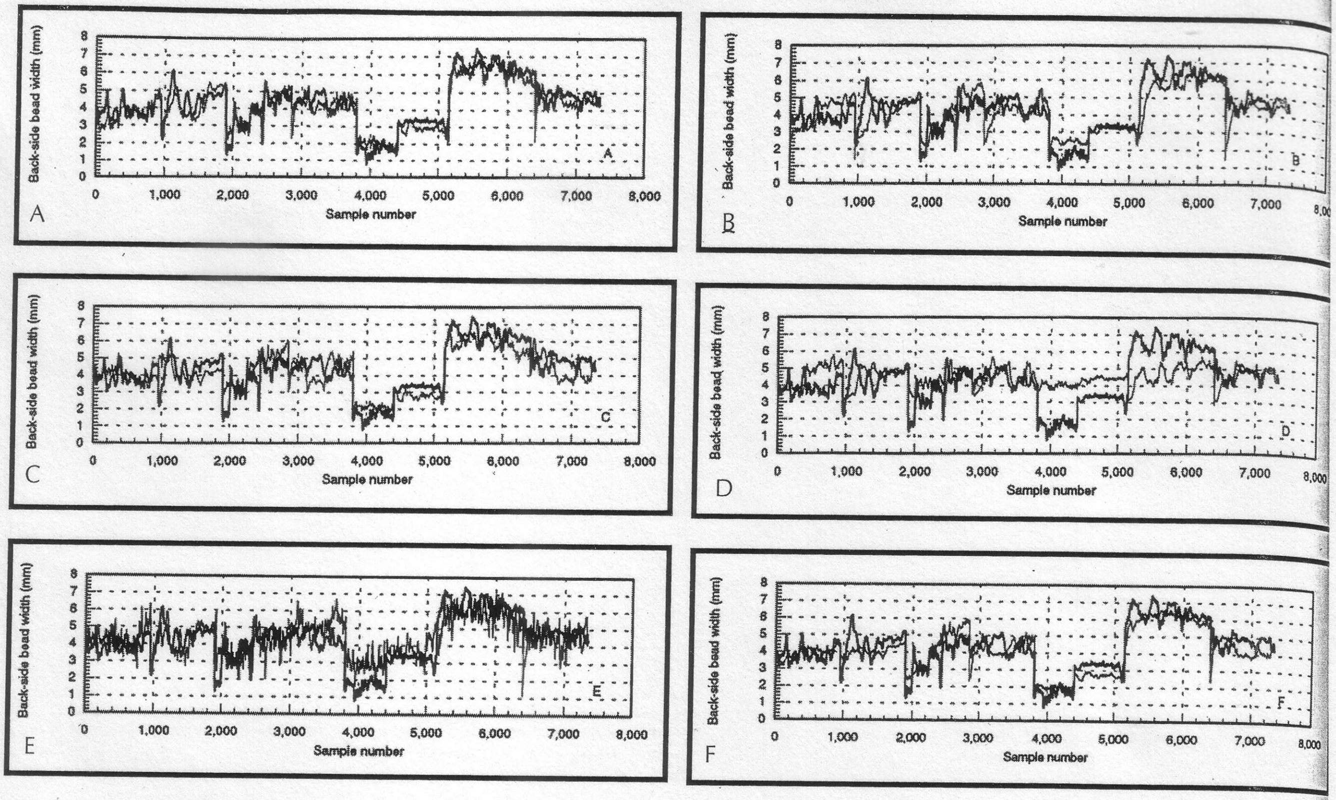

Fig. 11 — Experiments of neural network modeling of weld penetration using different weld pool parameters. A — Length, width and rear angles; B — length; C — width; D — length to width ratio; E — rear angles; F — length and width.

represents the visual geometrical characteristics of the pool. Thus, both size and shape information should be contained in the geometrical appearance parameters. Geometrical appearance parameters could consist of the shape and size parameters.

Size Parameters

The width and length are the size parameters of the weld pool. To examine the possibility of using the length or width of the weld pool to represent the weld penetration, two networks have been trained using the length and width as the input, respectively. The numbers of elements in the hidden layer in both cases are 500 because of Equation 4. The modeling results are illustrated in Fig. 11B and Fig. 11C, respectively. It can be seen that both the length and the width can provide rough estimates for the full penetration states. However, the modeling errors often exceed the 1-mm critical measurement.

Shape Parameters

It seems that the shape of the weld pool can be roughly characterized by using multiple size parameters. The ratio between the length and width of the pool provides pure information on the shape. Using the length-to-width ratio as the input, a network has been trained. The modeling results are plotted in Fig. 11D. It is apparent that the ratio cannot provide any useful weld penetration information. In order to explore the relationship between the pool shape and weld penetration, a more accurate description of the shape of the weld pool must be used.

The proposed rear angles can be used to characterize the shape of the weld pool. Nine rear angles can provide much more accurate shape information than the ratio. If the shape of the weld pool really contains sufficient information on the full penetration, an adequate estimation of the backside bead width should

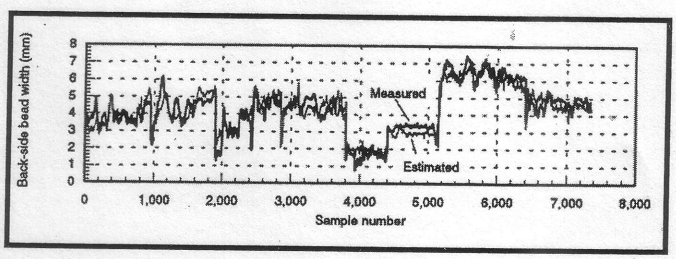

Fig. 12 — Neural network modeling of full penetration. The length and rear angles of the weld are used as the inputs of the neural network. The small difference between the measured and network estimated backside bead width, as observed in the figure, shows that the accuracy of the proposed monitoring approach for the full penetration is sufficient despite the variations in the welding conditions.

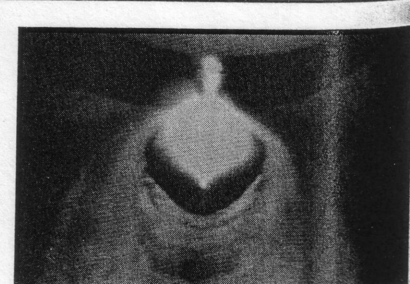

Fig. 13 — The arc appearance and the weld pool. The image shows that the arc covers the transverse span of the weld pool. The image is captured by using a slower shutter speed than was used for Fig. 2 images.

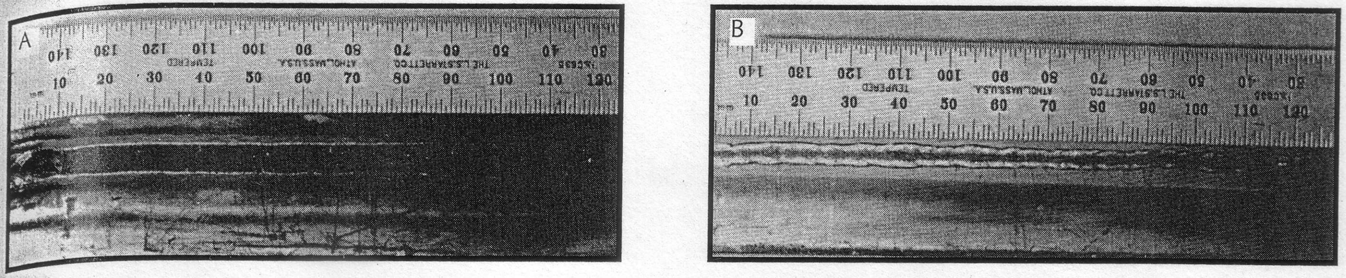

Fig. 14 — Dissimilar trends in top and backside bead widths. The top and backside appearances of a weld show that the backside bead width does not correlate with the top weld width. A — Top weld appearance; B — backside weld appearance.

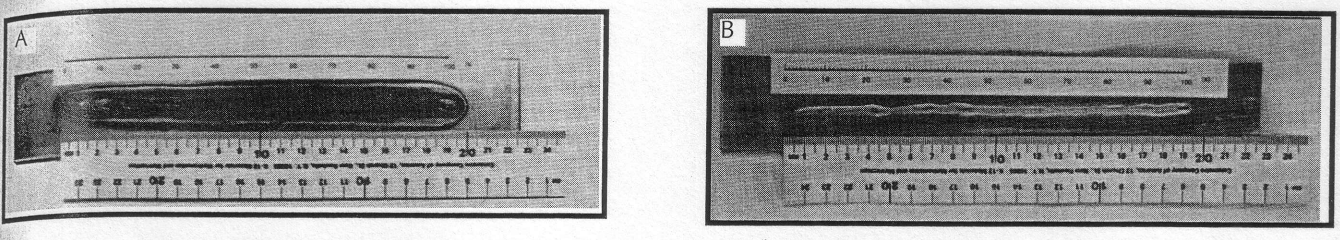

Fig. 15 — Weld with arc length variation. Current = 100 A, travel speed = 1.9 mm/s, bead-on-plate, rate of argon flow 30 ft^3/h. The arc length variation is shown in Fig. 3A. A — Top weld appearance. B — backside weld appearance.

be generated from the rear angles using a neural network. As shown in Fig. 11E, although the observed results are more accurate than the ratio's results, the modeling accuracy is still not sufficient. Furthermore, when both the ratio and appearance angles are used, the modeling accuracy is not improved. Thus, it seems that the shape of the weld pool does not contain sufficient information on the full penetration.

Geometrical Appearance Parameters

The geometrical appearance parameters may be acquired by incorporating multiple size parameters, or by incorporating the size and shape parameters. The width and length of the weld pool characterize the geometrical appearance of the weld pool. However, the description is rough. An accurate description of the geometrical appearance can be generated by combining the rear angles with a size parameter.

Using the width and length of the weld pool as the inputs, a network has been trained. The modeling results can be seen in Fig. 11F. A noticeable improvement in the modeling accuracy, in comparison with cases using the size or shape parameters, has been obtained. In Fig. 12, the modeling results using the rear angles and length of the weld pool are illustrated. The improvement of the accuracy is significant. This improvement is achieved by the more accurate description of the geometrical appearance of the weld pool.

Geometrical appearance of the weld pool can also be characterized by the width and rear angles. But, the most accurate results are provided by the length and rear angles. Also, compared with Fig. 11A where the width has been used in addition to the length and rear angles, no noticeable difference can be observed. This implies that the length and rear angles of the weld pool contain sufficient information on the weld penetration. Extra parameters may not be required for determining the weld penetration.

Discussions

The roles of most welding parameters in determining the weld penetration have been extensively investigated (Refs. 24, 37–39). If their roles in determining the parameters of the weld pool are known, the above trends of the correlation between the weld penetration and the weld pool parameters will be understood.

Current

It is known that the weld penetration is nearly proportional to the welding current. In fact, the Lorentz force is proportional to the current. Thus, the stirring of the liquid metal in the weld pool will be increased with an increase in the welding current (Ref. 25). Also, the impact of the plasma jets on the weld pool is increased with the current (Ref. 40). As a result, an increase in the current will generate an increase in the weld penetration. In order to determine the weld penetration from the geometrical appearance of the weld pool, the corresponding change in the shape and size of the weld pool must be found.

The images in Fig. 2 illustrate the appearance of weld pools made using different welding currents. It can be seen that the length of the weld pool is signficantly increased with the current. However, the increase in the width of the weld pool is much less significant.

It is known that the welding current is one of the critical welding parameters that determines the geometrical appearance of the weld pool. An increase in welding current produces an increase in power density (Ref. 41). The size of the weld pool, for example, the pool width and length, increases with the current. It was shown that the magnitude of the heat flux is dominated by the current (Ref. 42).

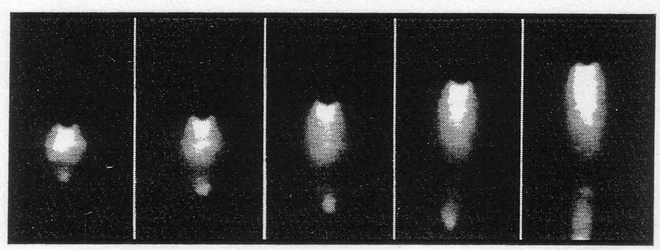

Fig. 16 — Arc distribution for different arc lengths. Current, 100 A, travel speed 1.9 mm/s, rate of argon flow = 30 ft^3/h, arc length from 2 mm to 4.5 mm, no laser illumination.

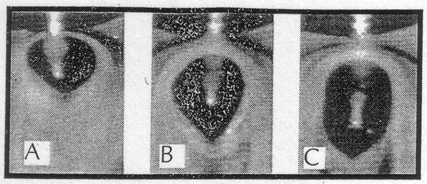

Fig. 17 — Weld pools for different arc lengths. Current 100 A, travel speed 1.9 mm/s, bead-on-plate, rate of argon flow = 30 ft³/h. A — Arc length = 2 mm. B — arc length = 3.5 mm. C — arc length = 4.5 mm.

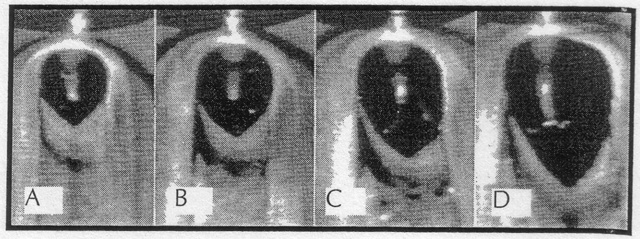

Fig. 18 — Weld pools for different travel speeds. Current, 100 A, arc length = 3 mm, rate of argon flow = 30 ft³/h. A — Travel speed = 2.92 mm/s; B — travel speed = 2.41 mm/s; C — travel speed = 1.95 mm/s; D — travel speed =1.43 mm/s.

Thus, a larger weld pool can be expected for a larger current. The image in Fig. 13 shows that the span of the weld pool along the traverse direction is covered by the arc. This implies that the surface of the weld pool is directly made molten by the arc. The width of the weld pool is primarily determined by the arc distribution. When the current increases, the radial dimensional distribution parameter slightly increases (Ref. 42). Thus, the width of the weld pool slightly increases with the current. On the other hand, the heat intensity significantly increases with the current (Ref. 42). The temperature on the surface of the weld pool is therefore expected to increase with an increased current. Hence, the length of the weld pool significantly increases when the current increases, whereas the width of the weld pool only slightly increases.

In addition to the relatively low sensitivity to the current, the width of the weld pool is also less sensitive to the variations in other welding parameters or conditions which can change the weld penetration as shown in Ref. 43 — Fig. 10B, and 10C. Thus, as shown in Fig. 11C, the pool width alone may not be able to represent the weld penetration with sufficient accuracy under possible variations in welding parameters and conditions, as was expected previously. To further illustrate this, the top and bottom appearances, acquired from an experiment, shown in Fig. 14 are given. It is apparent that in this case, no correlation between the backside bead width and the pool width can be observed. Thus, the leng of the weld pool, which is more sensiti to the current and other welding par meters and conditions (Fig. 11B and C should be a useful parameter for dete mining the weld penetration.

Arc Length

An increase in the arc length will ge erate an increase in the arc voltage. It known that the magnitude of the heat flu is proportional to the arc voltage (Ref. 42 However, the distribution parameter i creases nearly linearly with the arc lengt (Ref. 42). Also, the arc efficiency η sub stantially decreases when the arc lengt increases (Ref. 44). Thus, the relationshi between the weld penetration and the ar

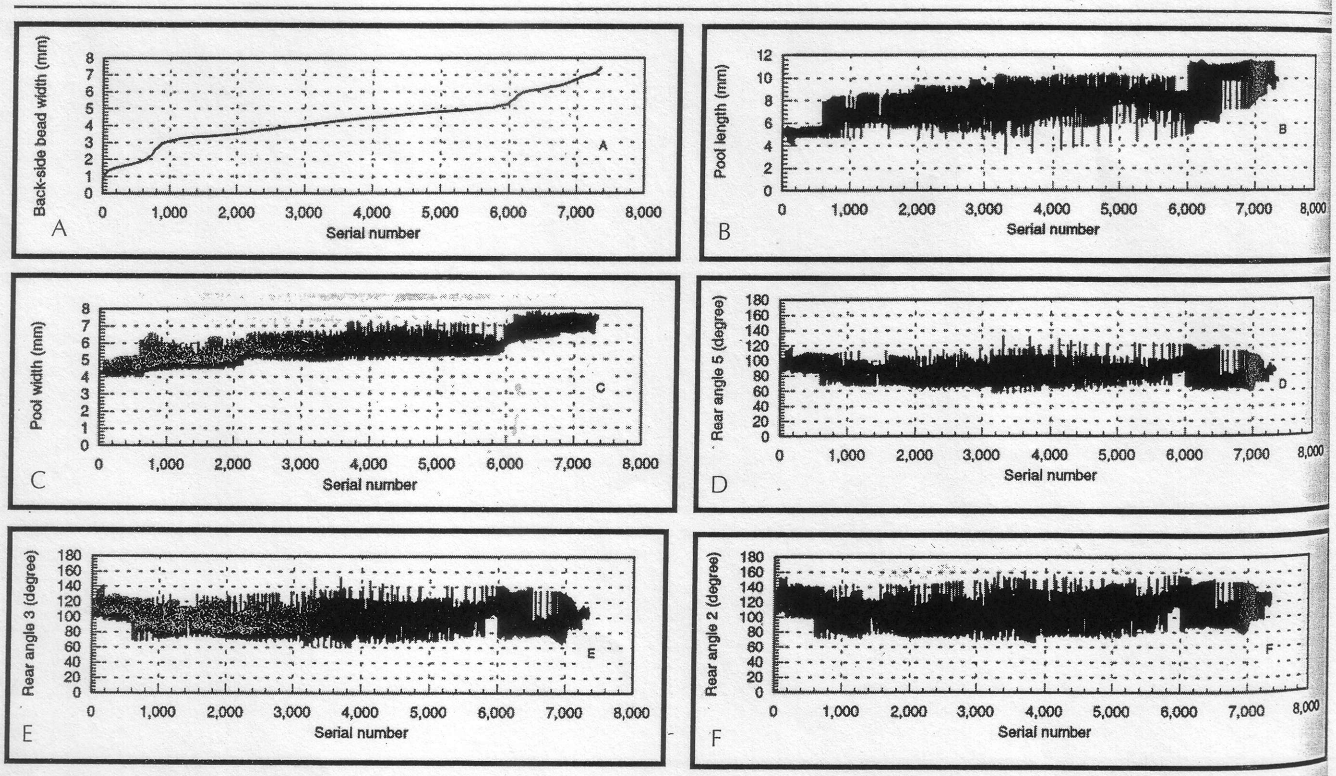

Fig. 19 — Trends of weld pool parameters with the weld penetration. The measurements of the backside bead width in Fig. 10A are rearranged with their values. The parameters of the weld are rearranged accordingly. A — Backside bead width; B — length of weld pool; C — width of weld pool; D — rear angle θ_5. E — rear angle θ_3; F — rear angle θ_2.

length seems to be complicated.

The topside and backside weld appearances of Experiment 1 are shown in Fig. 15A and B, respectively. The arc length increases from 2 to 4.5 mm during the experiment as shown in Fig. 3A. Because of the step change of the arc length, the irregularity of the weld can be observed. This irregularity can be more easily seen from the backside (Fig. 15B) than from the topside — Fig. 15A.

In the first 20 seconds, the arc length is 2 mm — Fig. 3A. The backside bead width is about 3.5 mm (Fig. 10A, B). At the transition from 2 mm to 2.5 mm, *i.e.*, around t = 20s, there is a peak in the backside bead width — Fig. 15B. Then the backside width roughly remains as it was during the first 20 seconds — Fig. 10A. After the transition from 2.5 to 3.5 mm, the backside bead width is about 4 mm. When the arc length is increased by 4 mm, the backside bead width slowly decreases to 3.3 mm. When the arc length becomes 4.5 mm, the backside bead width increases to about 4.5 mm. It can be seen that except for the peak at the transition zone caused by the step change of arc length, the weld penetration slowly increases with the arc length before the arc length reaches 3.5 mm. After 3.5 mm, the weld penetration starts to slowly decrease with the incremental arc length. However, when the arc length becomes 4.5 mm, the weld penetration increases again. The above observations are obtained based on Fig.10A and Fig. 3A and the backside appearance of the workpiece.

It is expected that the pool width increases with the arc length. However, in this experiment, the pool width remains almost unchanged before the arc length reaches 3.5 mm at t = 40s — Figs. 15A and 10 C. After the arc length reaches 3.5 mm, although the width of the heat-affected zone still increases with the incremental arc length (Fig. 15A), the pool width begins to decrease slowly. The pool width does not increase with increasing arc length. To explain this phenomenon, the arc distribution was observed for different arc lengths — Fig. 16. It was found that the arc distribution does not keep increasing with the arc length. Before the arc length reaches a critical value, the arc spread keeps increasing. Once the arc length exceeds the critical value, the arc spread begins to concentrate. In the experiment for Fig. 16, the critical value is 3.5 mm. Thus, despite the increase in the arc length beyond 3.5 mm, the pool width decreases. Also, because of the concentration of the arc, the backside bead width becomes large when the arc length is 4.5 mm, *i.e.*, from t = 80 to 100s — Fig. 15B.

Although the variations of the weld penetration in Experiment 1 cannot be predicted by the pool width, the weld pool geometrical appearance (Fig. 17) can be used to explain it. At t = 8s, the backside bead width is 3.5 mm. The pool is blunt and short (Fig. 17A). At t = 55s, the pool becomes longer and sharper — Fig. 17B. The backside bead width is 4 mm. When the time reaches 95s, the pool is very long — Fig. 17C. Thus, the backside bead width becomes 4.5 mm.

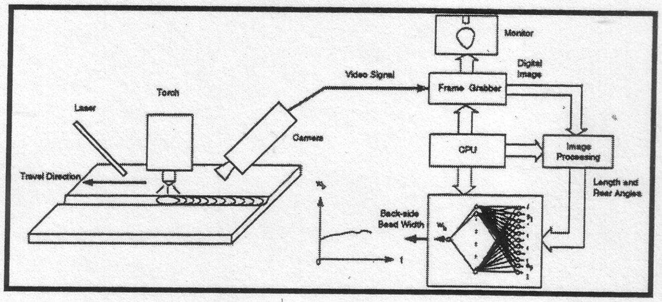

Fig. 20 — Real-time monitoring system for full penetration using weld pool appearance based on neural network.

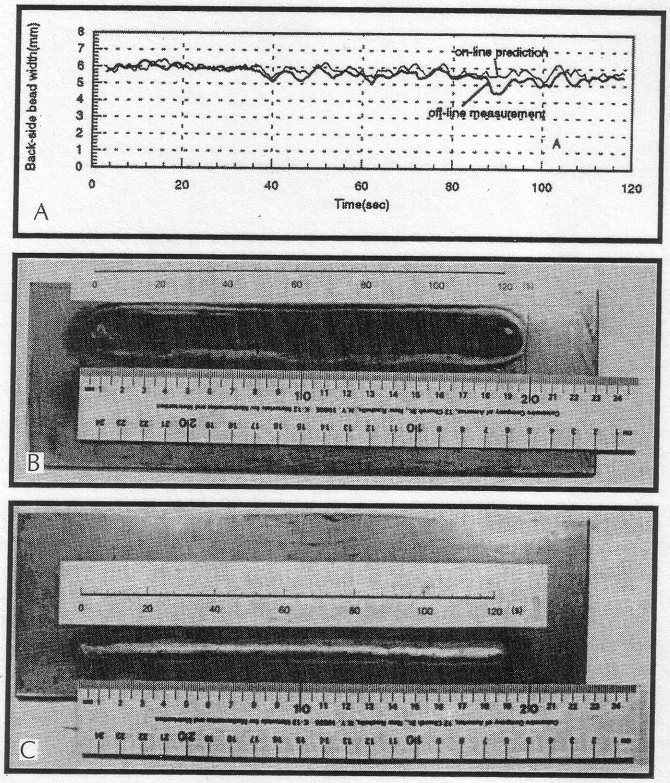

Fig. 21 — Full penetration real-time monitoring results. Current 100 A, arc length = 3 mm, travel speed = 1.53 mm/s, bead-on-plate, rate of argon flow = 30 ft³/h. A — On-line prediction of backside bead width in comparison with off-line measurement; B — top weld appearance; C — backside weld appearance.

Travel Speed

The weld penetration increases with decreasing travel speed. As it is known, at constant current and arc length, a slower travel speed arc will supply more heat input to the weldment and provide a higher peak temperature on the surface, whereas a faster one will cause less heat input and a lower peak temperature (Ref. 45). That is, a lower speed arc can be regarded as having a higher power density, since the distribution of the arc is not expected to be significantly affected by the travel speed. In order to link the geometrical appearance of the weld pool with the weld penetration, the influence of the travel speed on the size and shape of the weld pool should be studied.

The geometrical appearances of the weld pool corresponding to different travel speeds are shown in Fig. 18. When the arc travel speed is 2.92 mm/s, the size of the weld pool is small. By decreasing the travel speed to 2.41 mm/s, the weld pool is enlarged. However, the shape of the weld pool does not significantly change. This implies that the size of the weld pool is an important parameter to determine the weld penetration. When the travel speed decreases to 1.95 mm/s, the rear of the pool becomes sharper and the pool length is significantly increased. When the speed decreases to 1.43 mm/s, a very large increase in the length is observed. The rear of the weld pool becomes very sharp. Although the length of the weld pool may indicate the change in the travel speed, the accuracy in completely determining the weld penetration is still not sufficient. It can be seen that large modeling errors occur in the data corresponding to high travel speeds (see the range from 3800 to 4400 in Fig. 11B) if only the pool length is used because of the complexity of the relationship between the weld pool and weld penetration. Thus, by adding the rear angles, significant improvement in the modeling accuracy has been achieved. This improvement can be observed by comparing Fig. 11B with Fig. 12.

Trends

Figure 19A is generated from the measurements of the backside bead width given in Fig. 10A by rearranging the data incrementally. The length, width and a few rear angles of the weld pool plotted in Fig. 19B–F are the corresponding rearrangement from the original data. Although no exact relationship between the weld penetration and each individual parameter of the weld pool can be observed because the variations in the weld penetration are caused by changing different welding parameters, some rough trends can be observed.

In the small full penetration range, where the serial number is less than 600 in Fig. 19, the pool width and length almost do not change with the penetration. However, the rear angles do decrease when increasing the penetration. This may imply that the weld pool size cannot be used to predict the penetration variation when the full penetration is just established from the partial state. For example, the backside bead width varies from 1 to 2 mm in Experiment 5 (the sample number is from 3800 to 4400 in Fig. 10). The prediction given by the length or width of the weld pool are almost constant (Fig. 11B, C). Thus, it seems that the rear angles play important roles in determining the small full penetration.

When the degree of full penetration further increases, the pool length and the width begins to increase with the backside width. Roughly speaking, the length of the weld pool almost linearly increases with the backside bead width in the moderate full penetration range, *i.e.*, from 2 to 4.9 mm where the serial number in Fig. 19 is from 800 to 5000. The pool width also increases with the penetration in this range. However, the increase is step-like. In the serial number range from 800 to 2200, the pool width varies around 5 mm. In the serial number range from 2200 to 6000, the pool width fluctuates around 6 mm. No gradual increase with the penetration can be observed. This step-like relationship with the backside bead width makes it difficult to accurately predict the full penetration using only the pool width in the moderate full penetration range.

When the full penetration becomes very pronounced, a linear relationship between the backside bead width and pool width is observed. This can be seen when the serial number is larger than 6000 — Fig. 19A, C. In this range, the relationship between the pool length and weld penetration becomes complicated — Fig. 19A, B. Thus, the variation of the weld penetration in Experiment 7 can be much better tracked by the pool width than by the pool length — Fig. 11C, B. However, by incorporating the rear angles with the pool length, the weld penetration has been well tracked in this full penetration range.

The relationship between the rear angle $\theta_j (j = 1, 2, ..., 9)$ and weld penetration tends to become stronger as j decreases. For example, in the small serial number range, less that 600, θ_5 does not significantly change with the weld penetration (Fig. 19D), whereas θ_2 and θ_3 do decrease with weld penetration — Fig. 19E, F. This is understandable because the sharpness of the rear portion of the weld pool plays a more important role.

Before the backside bead width reaches 4 mm, *i.e.*, when the serial number is less than 3000, the rear angles decrease when the backside bead width increases. When the full penetration becomes more significant, the relationship tends to be complicated. However, this complexity does not mean that the correlation between the weld penetration and pool geometrical appearance becomes poorer. The weld penetration can still be determined with sufficient accuracy as it is in the small full penetration state — Fig. 12. This complexity is an inherent characteristic of the welding process. Because of this complexity, the neural network played an important role in correlating the weld penetration to the pool geometrical appearance.

Although the irregularity in the relationship between the full penetration state and individual pool parameter, a rough trend can still be observed. That is, no matter how the variation in the weld penetration is caused, the sharpness and size, including the length and width, of the weld pool tend to increase with the weld penetration.

Real-Time Monitoring

The full penetration has been monitored in real-time using the developed real-time image processing algorithm and trained neural network. The monitoring system is shown in Fig. 21. The inputs of the neural network are the length and rear angles of the weld pool. Since Professional II can provide the executive codes of the trained network as a subroutine which can be called by C program, the trained network can be loaded into the main program without additional programming.

The image processing for extracting the boundary of the weld pool can be completed in 100 ms. The network computation lasts less than 50 ms. Thus, with the consideration of the other possible computation, the weld penetration has been monitored at 5 Hz. This speed can be considered to be real-time for welding process control.

An example is given in Fig. 21. The current and travel speed are 100 A and 1.53 mm/s, respectively. The arc length is 3 mm. The on-line prediction of the backside bead width is plotted in Fig. 21A to examine the accuracy of the on-line prediction. In Figs. 21B and C, the appearances of the welds are illustrated. In this case, the variation in the weld penetration is caused by naturally occurring process variations, for example, the unavoidable variation in heat transfer condition along the weld. It can be seen that the variation of the backside bead width which specifies the full penetration has been monitored with sufficient accuracy.

Conclusions

The stainless steel 304 has been used to make bead-on-plate welds using direct current electrode negative (DCEN) gas tungsten arc welding (GTAW). The thickness of the material was 3 mm. Under these experimental conditions, it can be concluded that the geometrical appearance of the weld pool, specified by the length and rear angles, contains sufficient information on the weld penetration, judged by the 1-mm critical measurement of the modeling error. However, pure size or pure shape parameters only contain rough information on the weld penetration.

In addition, a real-time monitoring system has been developed to monitor the full penetration state, *i.e.*, the backside bead width. The high-shutter-speed camera assisted with the pulsating laser, the proposed real-time image processing algorithm, the relationship between the weld penetration and the geometrical appearance of the weld pool, and the neural network modeling capability play crucial roles in this achievement

Acknowledgment

This work is supported by the National Science Foundation under contract DMI9412637, and Allison Engine Corp., Indianapolis, Ind.

References

1. *ASM Handbook*. 1993. Vol. 6, Welding, brazing, and soldering, p. 1149.

2. Duley, W. W., and Mao, Y. L. 1994. Effect of surface condition on acoustic emission during welding of aluminum with CO_2 laser radiation. *Journal of Physics D: Applied Physics*, 27(7): 1379–1383.

3. Vilkas, E. P. 1966. Automation of gas tungsten-arc welding process. *Welding Journal* 45(5): 410-s to 416-s.

4. Suzuki, A., Hardt, D. E., and Valavani, L. 1991. Application of adaptive control theory to on-line GTA weld geometry regulation. *ASME Journal of Dynamics Systems, Measurement, and Control* 113(1): 93–103.

5. Bentley, A. E., and Marburger, S. J. 1992. Arc welding penetration control using quantitative feedback theory. *Welding Journal* 71(11): 397-s to 405-s.

6. Renwick, R. J., and Richardson, R. W. 1983. Experimental investigation of GTA weld pool oscillations. *Welding Journal* 62(2): 29-s to 35-s.

7. Zacksenhouse, M., and Hardt, D. E. 1983. Weld pool impedance identification for size measurement and control. *ASME Journal of Dynamic Systems, Measurement and Control* 105(3): 179–184.

8. Wang, Q. L., Yang, C. L., and Geng, Z. 1993. Separately excited resonance phenomenon of the weld pool and its application. *Welding Journal* 72(9): 455-s to 462-s.

9. Xiao, Y. H., and Ouden, G. den 1990. A study of GTA weld pool oscillation. *Welding Journal* 69(8): 289-s to 293-s.

10. Xiao, Y. H., and Ouden, G. den 1993. Weld pool oscillation during GTA welding of mild steel. *Welding Journal* 72(8): 428-s to 434-s.

11. Yoo, C. D. 1990. Effects of weld pool conditions on pool oscillation. Ph.D. dissertation, The Ohio State University, Columbus, Ohio.

12. Yoo, C. D., and Richardson, R. W. 1993. Experimental study on sensitivity and signal characteristics of weld pool oscillation. *Transactions of the Japan Welding Society* 24(2): 54–62.

13. Hardt, D. E., and Katz, J. M. 1984. Ultrasonic measurement of weld penetration. *Welding Journal* 63(9): 273s-281s.

14. Lott, L. A. 1984. Ultrasonic detection of molten/solid interfaces in weld pools. *Materials Evaluation* 42(3): 337–341.

15. Carlson, N. M., and Johnson, J. A. 1988. Ultrasonic sensing of weld pool penetration. *Welding Journal* 67(11): 239-s to 246-s.

16. Carlson, N. M., *et al.* 1992. Ultrasonic NDT methods for weld sensing. *Materials Evaluation* 50(11): 1338–1343.

17. Yang, J., *et al.* 1994. Ultrasonic weld penetration depth sensing with a laser phased array. *Proceedings of 1994 ASME International Mechanical Engineering Congress*, PED-Vol. 68-1, *Manufacturing Science and Engineering*, pp. 245–254.

18. Nagarajan, S., Chen, W. H., and Chin, B. A. 1989. Infrared sensing for adaptive arc welding. *Welding Journal* 68(11): 462-s to 466-s.

19. Nagarajan, S., Banerjee, P., Chen, W., and Chin, B. A. 1990. Weld pool size and position control using IR sensors. *Proceedings of NSF Design and Manufacturing Systems Conference*, Arizona State University.

20. Chen, W., and Chin, B. A. 1990. Monitoring joint penetration using infrared sensing techniques. *Welding Journal* 69(4): 18-s to 85-s.

21. Beardsley, H., Zhang, Y. M., and Kovacevic, R. 1994. Infrared sensing of welding parameters for weld penetration control. *International Journal of Machine Tool and Manufacturing* 34(8): 1079–1090.

22. Richardson, R. W., *et al.* 1984. Coaxial arc weld pool viewing for process monitoring and control. *Welding Journal* 63(3): 43–50.

23. Hoffman, T. 1991. Real-time imaging for process control. *Advanced Material & Processes* 140(3): 37–43.

24. Rokhlin, S. I., and Guu, A. C. 1993. A study of arc force, pool depression, and weld penetration during gas tungsten arc welding. *Welding Journal* 72(8): 381-s to 390-s.

25. Lin, M. L., and Eagar, T. W. 1984. Influence of surface depression and convection on arc weld pool geometry. *Transport Phenomena in Materials Processing*, ASME, New York, N.Y., pp. 63–69.

26. Zhang, Y. M., *et al.* 1993. Determining joint penetration in GTAW with vision sensing of weld face geometry. *Welding Journal* 72(10): 463-s to 469-s.

27. Zhang, Y. M., Kovacevic, R., and Wu, L. 1996. Dynamic modeling and identification of gas tungsten arc welding process for weld penetration control. *ASME Journal of Engineering for Industry*, 118(1): 123–136.

28. Zhang, Y. M., Kovacevic, R., and Li, L. 1996. Adaptive control of full penetration GTA welding. *IEEE Transactions on Control Systems Technology, 4(4): 394-403.*

29. Kovacevic, R., and Zhang, Y. M. 1996. Real-time image processing for monitoring of free weld pool surface. To appear in *ASME Journal of Manufacturing Science and Engineering.*

30. Kovacevic, R., and Zhang, Y. M. 1996. Sensing free surface of arc weld pool using specular reflection: principle and analysis. To appear in *Proc. Instn Mech Engrs, Part B, Journal of Engineering Manufacturing*, Vol. 210.

31. Kovacevic, R., and Zhang, Y. M. 1996. Apparatus and method for measuring 3D weld pool shape. United States Patent, #5,481,085, January 2.

32. Kovacevic, R., Zhang, Y. M., and Ruan, S. 1995. Sensing and control of weld pool geometry for automated GTA welding. *ASME Journal of Engineering for Industry*, 117(2): 210–222.

33. Pandit, S. M., and Wu, S. M. 1983. *Time Series and System Analysis with Applications*, Chap. 2, John Wiley and Sons, New York, N.Y.

34. *Using NeuralWorks: Professional 11/Plus and NeuralWorks Explorer, NeuralWare Inc.* 1993. Pittsburgh, Pa.

35. Hunt, K. J., *et al.* 1992. Neural networks for control systems: a survey. *Automatica* 28(6): 1083–1112.

36. Zhang, Y. M., and Kovacevic, R. 1996. Real-time sensing of sag geometry during GTA welding. To appear in *ASME Journal of Manufacturing Science and Engineering.*

37. Burgardt, P., and Heiple, C. R. 1986. Interactions between impurities and welding parameters in determining GTA weld shape. *Welding Journal* 65: 150-s to 155-s.

38. Shirali, A. A., and Mills, K. C. 1993. The effect of welding parameters on penetration in GTA welds. *Welding Journal* 71(7): 347-s to 353-s.

39. Metzbower, E. A. 1993. Penetration depth in laser beam welding. *Welding Journal* 71(8): 403-s to 407-s.

40. Friedman, E. 1978. Analysis of weld puddle distortion and its effect on penetration. *Welding Journal* 57(6): 161-s to 166-s.

41. *Welding Handbook*. 1987. Eight edition, Vol. 1, American Welding Society, Miami, Fla. pp. 69–71.

42. Tsai, N. S., and Eagar, T. W. 1985. Distribution of the heaty and current fluxes in gas tungsten arcs. *Metallurgical Transactions B*, Vol. 16B, pp. 841–846.

43. Zhang, Y. M., Kovacevic, R., and Wu, L. 1992. Sensitivity of front-face weld geometrical parameters in representing weld penetration. *Proc Instn Mech Engrs, Part B, Journal of Engineering Manufacture* 206 (3): 191–197.

44. Giedt, W. H., Tallerico, L. N., and Fuerschbach, P. W. 1989. GTA welding efficiency: calorimetric and temperature filed measurements. *Welding Journal* 68(1): 28-s to 32-s.

45. Kraus, H. G. 1989. Surface temperature measurement of GTA weld pools on thin-plate 304 stainless steel. *Welding Journal* 68(3): 84-s to 91-s.